

Inverse design of directional hybrid nanoantennas using neural networks

Ru-Lin Guan(管如林), Deng-Chao Huang(黄登朝), Ya-Qiong Li(李雅琼), Cheng Wang(王晨), and Bin-Zi Xu(徐彬梓)

Citation: Chin. Phys. B, 2025, 34 (**9**): 090702. DOI: 10.1088/1674-1056/adeb5c
http://cpb.iphy.ac.cn; http://iopscience.iop.org/cpb

What follows is a list of articles you may be interested in

Graph neural networks unveil universal dynamics in directed percolation

Ji-Hui Han(韩继辉), Cheng-Yi Zhang(张程义), Gao-Gao Dong(董高高), Yue-Feng Shi(石月凤), Long-Feng Zhao(赵龙峰), and Yi-Jiang Zou(邹以江)

Chin. Phys. B, 2025, 34 (**8**): 080702. DOI: 10.1088/1674-1056/add505

Analysis and design of multivalued many-to-one associative memory driven by external inputs

Qiang Fang(方强) and Hao Zhang(张浩)

Chin. Phys. B, 2025, 34 (**8**): 080701. DOI: 10.1088/1674-1056/add24b

Advances in neuromorphic computing: Expanding horizons for AI development through novel artificial neurons and in-sensor computing

Yubo Yang(杨玉波), Jizhe Zhao(赵吉哲), Yinjie Liu(刘胤洁), Xiayang Hua(华夏扬), Tianrui Wang(王天睿), Jiyuan Zheng(郑纪元), Zhibiao Hao(郝智彪), Bing Xiong(熊兵), Changzheng Sun(孙长征), Yanjun Han(韩彦军), Jian Wang(王健), Hongtao Li(李洪涛), Lai Wang(汪莱), and Yi Luo(罗毅)

Chin. Phys. B, 2024, 33 (**3**): 030702. DOI: 10.1088/1674-1056/ad1c58

Silicon-based optoelectronic synaptic devices

Lei Yin(尹蕾), Xiaodong Pi(皮孝东), Deren Yang(杨德仁)

Chin. Phys. B, 2020, 29 (**7**): 070703. DOI: 10.1088/1674-1056/ab973f

An artificial synapse by superlattice-like phase-change material for low-power brain-inspired computing

Qing Hu(胡庆), Boyi Dong(董博义), Lun Wang(王伦), Enming Huang(黄恩铭), Hao Tong(童浩), Yuhui He(何毓辉), Ming Xu(徐明), Xiangshui Miao(缪向水)

Chin. Phys. B, 2020, 29 (**7**): 070701. DOI: 10.1088/1674-1056/ab892a

---

Inverse design of directional hybrid nanoantennas using neural networks

Ru-Lin Guan(管如林)[1,2], Deng-Chao Huang(黄登朝)[1,2,†], Ya-Qiong Li(李雅琼)[1,2], Chen Wang(王晨)[1,2], and Bin-Zi Xu(徐彬梓)[1,2]

[1] *Key Laboratory of Advanced Perception and Intelligent Control of High-End Equipment, Ministry of Education, College of Electrical Engineering (College of Integrated Circuits), Anhui Polytechnic University, Wuhu* 241000, *China*

[2] *Anhui Engineering Research Center of Vehicle Display Integrated Systems, School of Integrated Circuits, Anhui Polytechnic University, Wuhu* 241000, *China*

(Received 3 April 2025; revised manuscript received 1 July 2025; accepted manuscript online 3 July 2025)

Controlling the directionality of quantum emitter (QE) radiation is crucial for advancing nanophotonic devices, yet designing compact, single nanoantennas for this purpose remains challenging with traditional methods due to computational demands and optimization complexity. This paper introduces a neural-network-based inverse design approach to efficiently optimize single core–shell nanosphere antennas and their derivatives — notched core–shell structures and dimers — for highly directional QE emission. We systematically compare the radial basis function (RBF), support vector regression (SVR), and backpropagation neural network (BPNN) algorithms. Our results demonstrate BPNN's superior performance in accurately mapping nanoantennas' geometric and material parameters to their far-field radiation characteristics. Subsequent BPNN-driven optimization confirms that all three investigated structures (single core–shell, notched core–shell, and dimer) can achieve robust directional emission. This is accomplished by precisely exciting higher-order electric and magnetic multipoles engineered to possess equal amplitudes and opposite phases, thereby facilitating directional radiation from QEs and enabling more efficient nanophotonic device design.

Keywords: artificial neural network, Kerker condition, nanosphere nanoantenna, high-order plasmon modes

PACS: 07.05.Mh, 42.25.–p, 73.20.Mf, 73.20.Mf

DOI: 10.1088/1674-1056/adeb5c **CSTR:** 32038.14.CPB.adeb5c

1. Introduction

Optical nanoantennas can enhance and flexibly manipulate light at dimensions far smaller than the free-space wavelength. This property offers unique opportunities for applications including sensors,[1] optoelectronic devices,[2] biomedical imaging,[3] optical signal processing,[4] photocatalysis,[5] and quantum optics.[6] In the optical frequency range, optical wireless nanolink systems can collect energy radiated by individual quantum emitters, thereby enabling efficient single-photon sources. Furthermore, highly directional receiving nanoantennas are powerful tools for achieving exceptionally high local field gradients. In the field of nanophotonics, arrays of plasmonic or dielectric nanoantennas based on the Yagi–Uda design have achieved notably high directionality, both theoretically and experimentally.[7] Such nanoantennas consist of several small scatterers, and their operating principle resembles that of their radio-frequency counterparts. Recent investigations have explored Yagi–Uda nanoantennas composed of different scatterers, such as core–shell nanoparticles,[8] plasmonic nanoparticles,[9] and high-refractive-index dielectric nanoparticles.[10] Regardless of the scatterer type, these nanoantennas exhibit high directionality over a relatively wide frequency range. However, their radiation pattern is determined by fixed geometric parameters. Precise nanoscale control over the spacing and symmetry of reflectors, drivers, and directors is required, often making these directional array antennas difficult to manufacture and relatively large compared to the operating wavelength. Additionally, current nanofabrication technologies struggle with high-precision, large-scale production. Consequently, achieving miniaturized and simplified directional nanoantennas remains a significant challenge and an active area of research.

Classical antenna theory offers a potentially simpler and more efficient approach for creating highly directional nanoantennas. This method involves rapidly generating spatially oscillating currents within a subwavelength region. Doing so excites higher-order electromagnetic multipole moments within the nanoantenna, which can achieve ultrahigh directionality (e.g., directivity > 10).[11] Recent studies have demonstrated that exciting magnetic dipole resonances within nanospheres enhances directionality without significantly increasing antenna size.[12] Furthermore, exciting magnetic quadrupole modes can provide even greater directionality compared to magnetic or electric dipoles.[13,14] Currently, single multilayer core–shell nanosphere antennas can produce reasonably good directional radiation. This is accomplished by tuning Mie scattering coefficients — through variations in core/shell materials and thicknesses — to induce phase inversion between high-

[†]Corresponding author. E-mail: huangdengchao@ahpu.edu.cn

© 2025 Chinese Physical Society and IOP Publishing Ltd. All rights, including for text and data mining, AI training, and similar technologies, are reserved.

order electric and magnetic multipoles. However, optimizing these core–shell nanospheres to control fluorescence or quantum emitter radiation directionality is complex. This optimization process involves managing a large number of dimensional and material parameters and necessitates lengthy electromagnetic computation times. These factors hinder the development and application of such directional nanoantennas.

In recent years, the rapid development of artificial intelligence has enabled the efficient analysis of nanophotonic structures. Machine learning algorithms, trained on large datasets, can accurately capture the complex physical relationships between semiconductor/metal nanostructures and their electromagnetic responses. These algorithms are widely applied in nanophotonics, particularly for designing metasurfaces and predicting the scattering, transmission, and reflection spectra of plasmonic systems.[15] For instance, recent research indicates that deep neural networks (DNNs) can predict the near-field characteristics of dielectric nanostructures by training on electric field intensity data.[16] Convolutional neural networks (CNNs) have been used to predict 2D electric field distributions in plasmonic nanoparticles,[17] while artificial neural networks (ANNs) can predict the near-field and far-field characteristics of 3D nanoantennas.[18] Therefore, employing neural network algorithms can effectively address the challenges of excessive computation time and complex optimization associated with multilayer core–shell nanosphere antennas. Among these regression algorithms, the backpropagation (BP) neural network, a classic deep learning algorithm, is selected for its flexible architecture and excellent nonlinear fitting capabilities, making it highly suitable for establishing the complex nonlinear relationship between the dimensional features of nanoantennas and their optical responses. Support vector regression (SVR), a powerful and widely used kernel-based method, is included for its strong generalization performance, particularly when training with high-dimensional data or limited datasets. The radial basis function (RBF) network, another established neural network, typically features a simpler architecture and faster training speeds compared to the more complex backpropagation neural network (BPNN) algorithm, and it often performs well in interpolation tasks. Collectively, these three algorithms exemplify the current application and performance of neural network approaches in the design and optimization of micro/nanoscale devices.

In this paper, we aim to further enhance the directionality and front-to-back ratio of single multilayer core–shell nanosphere antennas by introducing perforations (thereby creating notched core–shell structures) and by constructing dimers. Simultaneously, we employ three neural network algorithms — RBF regression,[19] SVR,[20] and BPNN regression[21] — to optimize the far-field directionality of these three nanoantenna types (single core–shell, notched core–shell, and core–shell dimer) under quantum emitter illumination. Through a performance comparison, we find that the BPNN provides optimal error control with the least training time. Using the optimized BPNN algorithm, we identify the ideal distance between the quantum emitter and the nanoantenna, along with the optimal dimensional parameters for the antennas. Under these optimized conditions, all three nanosphere antenna types demonstrate effective control over quantum emitter radiation directionality by exciting higher-order electric and magnetic multipoles with equal amplitudes and opposite phases. Notably, the notched core–shell nanosphere antenna achieves a directivity of 14, surpassing that of typical metallic Yagi–Uda array antennas. Furthermore, compared to single-material dimers, the core–shell nanosphere dimer antenna demonstrates superior directionality, exhibiting a front-to-back ratio exceeding 60 at a wavelength of 750 nm. The approach presented herein, combining BPNN design with structural modifications, offers a new direction for the design of complex nanoantenna structures.

2. Results and discussion

2.1. Methods

Our study investigates the electromagnetic properties of core–shell nanospheres, notched core–shell nanospheres, and nanosphere dimers, with a focus on their spectral behavior in the far-field region. To analyze their optical behavior, we employ a simulated quantum source, represented by an electric dipole, to excite their optical responses. The simulations were performed using the finite element method (FEM) implemented in CST Studio Suite 2023. In these simulations, a coarse grid with a spacing of 2 nm was used in the background region, while the grid spacing for the nanoantenna structure was set to 0.4 nm. The grid within the nanogap region utilized adaptive meshing with a minimum spacing of 0.05 nm. Perfectly matched layer (PML) boundary conditions were applied on all sides of the simulation domain. These boundary conditions effectively absorb outgoing electromagnetic waves, preventing artificial reflections and ensuring accurate simulation of an open-space environment. The dipole source was simulated by connecting two perfect electric conductor (PEC) metallic nanoparticles with a discrete port. The dielectric environment surrounding the nanoantenna was set to vacuum. An excitation wavelength range of 300–1200 nm was chosen to comprehensively study the electromagnetic responses across a broad spectral range. This approach enabled a detailed analysis of the electromagnetic behavior of core–shell nanospheres and their derived models, capturing variations in angular patterns and near-field intensity distributions. Specifically, the simulations recorded the total-field scattered-field (TFSF) from the inhomogeneous core–shell nanospheres and

their derived models, providing critical insights into field confinement and enhancement by tracking key electromagnetic field components. To validate mesh convergence, we systematically refined the mesh for the same model while keeping all other parameters constant. Key output parameters, such as far-field directivity and near-field intensity, were closely monitored between successive refinements. We ensured that the variation in these output parameters between two consecutive mesh refinements did not exceed 2%.

The microscopic geometry of semiconductor and metal nanoparticle antennas exhibits a highly nonlinear and often unpredictable relationship with their electromagnetic responses. To explore this complex relationship, this paper investigates ways to effectively capture the implicit correlations between antenna geometry and far-field data by training RBF, SVR, and BPNN data regression algorithms. Through data preprocessing, model training, and computational error analysis, combined with carefully selected nanosphere radius structures, we demonstrate the superiority of our proposed approach in accurately predicting far-field directionality and front-to-back ratios.

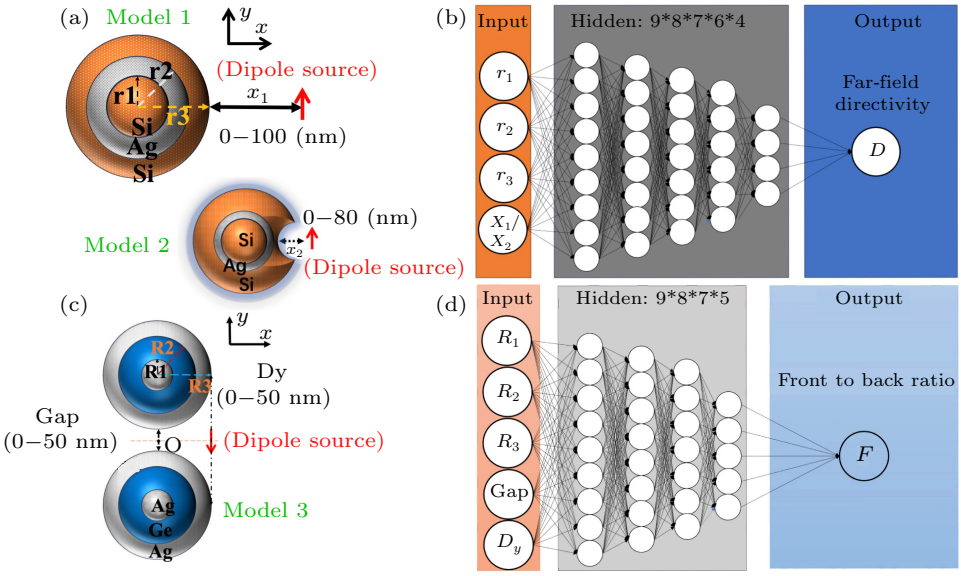


Fig. 1. (a) Schematic diagram of a quantum source exciting a single core–shell nanosphere, a notched nanosphere and (c) a coupled nanosphere dimer. (b) Using BPNN to predict the far-field directionality of a single nanosphere and a notched nanosphere under quantum source irradiation with different size parameters. (d) Using BPNN to predict the far-field directionality of a coupled nanosphere dimer under quantum source irradiation with different size parameters.

Table 1. BPNN input parameter settings.

Model	Model 1/model 2				
Parameters	r_1	r_2	r_3	x_1	x_2
Value (nm)	25–35	100–185	190–210	0–100	0–80
Model	Model 3				
Parameters	R_1	R_2	R_3	Gap	D_y
Value (nm)	20–40	195–205	230–240	0–50	0–60

The three types of nanoantenna structures studied in this paper, including core–shell nanospheres, notched core–shell nanospheres, and core–shell nanosphere dimers, are shown in Fig. 1. We first employed the BPNN algorithm to predict the directionality of these three types of nanoantennas under quantum source illumination. The parameter settings for the BPNN are shown in Table 1. Here, r_1, r_2, r_3 and R_1, R_2, R_3 represent the radii of the different material layers of each core–shell nanosphere; x_1 and x_2 represent the distances between the quantum source and the surface of the core–shell nanosphere; gap and D_y represent the nanogap width of the nanosphere dimer and the offset distance of the quantum source relative to the horizontal line $y = 0$, respectively. We employed the forward propagation method within the BPNN algorithm to output the directionality of the three nanoantenna structures. Simultaneously, we utilized BP to calculate the error between the true values and the predicted values. Subsequently, based on the error matrix, we calculated the error gradients for each parameter using the chain rule. To enhance the computational efficiency of the entire neural network during BP, we also incorporated the ReLU activation function[22]

$$\text{Relu} = \begin{cases} x, & x > 0, \\ 0, & x \le 0. \end{cases} \tag{1}$$

In order to minimize the difference between the predicted value and the true value, we adjusted the parameters of the hidden layer in the neural network. The settings of the hidden layers in the BPNN are shown in Figs. 1(b) and 1(d). Our optimization goals are far-field directionality and the front-to-back ratio of the radiation. We found that the BPNN algorithm is highly effective in predicting the far-field radiation performance of core–shell nanosphere nanoantennas with vary-

ing size parameters, demonstrating a close agreement between predicted and true values. Figure 2 compares the far-field directionalities of three types of nanoantenna structures — core–shell nanospheres, notched core–shell nanospheres, and core–shell nanosphere dimers — under electric dipole source illumination. This comparison showcases the far-field directionality predicted by the BPNN algorithm alongside the actual far-field directionality.

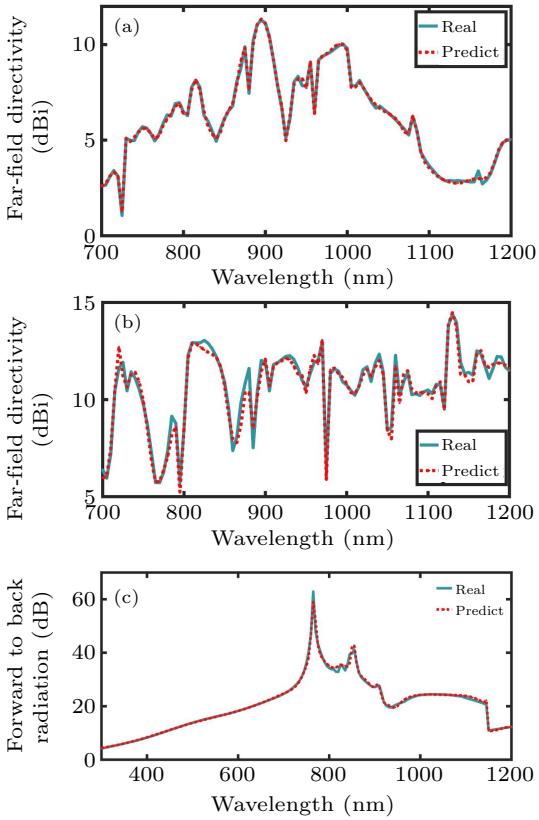


Fig. 2. Far-field directivity of silver–germanium–silver nanospheres (a) and notched silver–germanium–silver nanospheres (b) under electric dipole irradiation; (c) front-to-back radiation ratio of nanosphere dimers.

2.2. Numerical simulation of the near-electric field

To further investigate the relationship between the far-field response of core–shell nanosphere antennas and the relative positions of excitation sources within the antenna system, as well as the structural size parameters of the antennas, we introduced RBF and SVR algorithms for comparative study. We will now detail the specific applications of the RBF data regression algorithm and the SVR data regression algorithm in this study. The RBF data regression algorithm is a commonly used machine learning algorithm for classification and regression problems. We utilized a Gaussian kernel function to establish the relationship between the size parameters of the three nanosphere antennas, the relative positions of the excitation source, and the far-field directionality of the antenna system. The Gaussian kernel function is as follows:

$$K(x,y) = \exp\left(-\frac{\|x-y\|^2}{2\sigma^2}\right). \tag{2}$$

Here, $\|x-y\|^2$ represents the Euclidean distance between the nanoantenna input vector x and the output vector y, while σ is the kernel parameter used to control the width of the Gaussian kernel function. The SVR framework, an extension of the support vector machine (SVM) method used for regression tasks, is applied to handle high-dimensional nonlinear relationships in the dataset. The hyperplane equation is used in the SVR algorithm to establish the relationship between the size parameters of the three nanosphere antennas, the relative positions of the excitation source, and the far-field directionality of the antenna system. The equation for the hyperplane is

$$\omega^{\mathrm{T}} x + b = 0, \tag{3}$$

where ω is the normal vector of the hyperplane and b is the intercept. The constraints of this algorithm are

$$y\left(\omega^{\mathrm{T}} x + b\right) \geq 1 - \xi_i, \quad \xi_i \geq 0. \tag{4}$$

Here, ξ_i is the sample as a whole and cannot be too large. It is reflected as follows:

$$\min \frac{1}{2}\omega^{\mathrm{T}}\omega + C\sum_i \xi_i, \tag{5}$$

where C is the penalty coefficient, and its coefficient and the RBF parameter selection control the data regression performance of the SVR algorithm. Furthermore, we employed regularization techniques to prevent overfitting of the data and improve the generalization ability of this algorithm.

In order to compare the performance of the three algorithms, we added the mean absolute error (MAE),[23] mean bias error (MBE),[24] and root-mean-square error (RMSE)[25] for comparison. The calculation formulas for the three errors are

$$\mathrm{MAE} = \frac{1}{m}\sum_{i=1}^{m} |y_i - \hat{y}_i|, \tag{6}$$

$$\mathrm{MBE} = \frac{1}{m}\sum_{i=1}^{m} (y_i - \hat{y}_i), \tag{7}$$

$$\mathrm{RMSE} = \sqrt{\frac{1}{m}\sum_{i=1}^{m} (y_i - \hat{y}_i)^2}, \tag{8}$$

where m is the number of samples in the far-field dataset of the antenna system, y_i is the true value of the ith sample, and $\hat{y}_i$ is the predicted value of the ith sample. We used the RMSE to measure the deviation between the true and predicted values of the antenna's far-field training and test datasets. The closer these three types of errors are to zero, the better the far-field performance of the antenna predicted by the algorithm's data regression. To better discuss the accuracy between the true and predicted values of nanoantennas, we also included the correlation coefficient R,[26]

$$R = \frac{\sum_{i=1}^{n}(x_i - \bar{x})(y_i - \bar{y})}{\sqrt{\sum_{i=1}^{n}(x_i - \bar{x})^2 \sum_{i=1}^{n}(y_i - \bar{y})^2}}. \tag{9}$$

The closer R is to one, the more accurate the far-field performance data prediction.

We preprocessed the far-field data results of the three types of nanoantennas obtained from CST electromagnetic simulation calculations. Specifically, based on the nanoantenna size parameters and quantum source relative position parameters listed in Table 1, we performed electromagnetic simulation calculations, resulting in the following data: 6100 sets and 6060 sets of far-field directionality data for model 1 and model 2 antenna systems in the wavelength range of 700 nm to 1200 nm, and 21720 sets of far-field radiation front-to-back ratio data in the wavelength range of 300 nm to 1200 nm. For each type of antenna system, we used the first 70% of its far-field data as the training set and the last 30% as the test set for regression analysis.

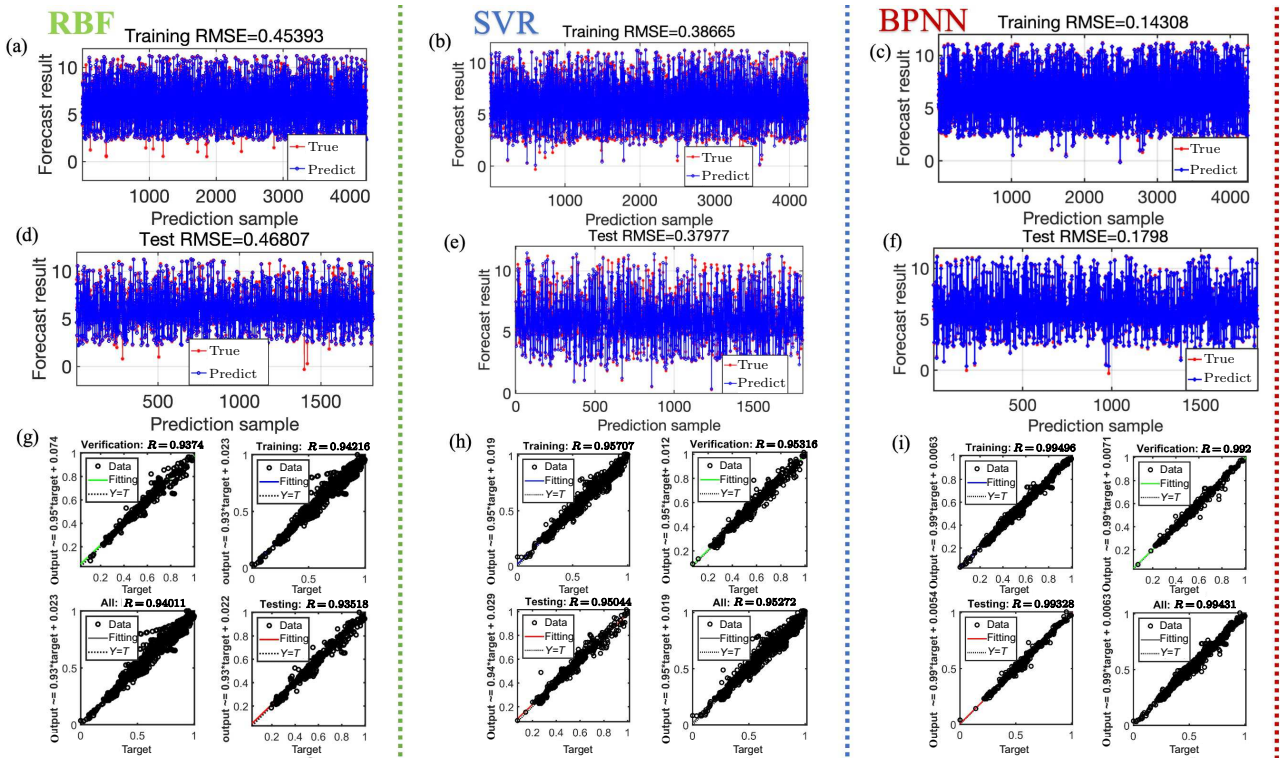


Fig. 3. Three regression algorithms (RBF, SVR, and BPNN algorithms) trained on the model 1 far-field radiation dataset. (a)–(c) Training set RMSE errors, (d)–(f) test set RMSE errors, (g)–(i) R values.

To evaluate the prediction performance of the three regression algorithms for the far-field directionality of core–shell nanosphere antennas with varying size parameters, we consistently processed the far-field radiation data of the model 1 antenna system using these three regression algorithms. The 6100 sets of far-field radiation data, spanning the wavelength range of 300 nm to 700 nm, were divided into two groups: the first 4242 sets forming the training set, and the subsequent 1818 sets serving as the test set. The input and output parameters were set as shown in Fig. 1 and Table 1. Figure 3 shows the RMSE and R values of the three regression algorithms (the RBF, SVR, and BPNN algorithms) trained using the model 1 far-field radiation dataset. When employing the RBF algorithm, we first normalized the data and set the spread rate of the RBF to 0.18 distance/second. Upon calculation, the RBF algorithm yielded the following errors for the training set: RMSE = 0.45393, MAE = 0.21283, MBE = 0.029624. The accuracy of the training set was as follows: correlation coefficient $R = 0.94216$. For the test set, the errors were RMSE = 0.46807, MAE = 0.25867, MBE = 0.016282, and the accuracy was $R = 0.93518$. Next, when using the SVR algorithm, we set the penalty factor $C = 16$ and the RBF parameter to 225. After running for 38.72 seconds, the training set errors were RMSE = 0.38665, MAE = 0.27736, MBE = 0.0011415, and the training set accuracy was $R = 0.95707$. The test set errors were RMSE = 0.37977, MAE = 0.29853, MBE = 0.0031622, and the test set accuracy was $R = 0.95044$. Finally, we used the BPNN algorithm to predict the far-field radiation performance of model 1. We set five hidden layers (with nine, eight, seven, six, and four nodes, respectively; the numbers of hidden layer nodes are discussed in detail in subsequent sections), 1000 iterations, an error threshold of 10^{-6}, and a learning rate of 0.01. After 45.112 seconds of training, the BPNN algorithm's training set errors were RMSE = 0.14308, MAE = 0.10038, MBE = 0.00096157, and the training set accuracy was $R = 0.99496$. The test set errors were RMSE = 0.1798, MAE = 0.11597, MBE = 0.0065716, and the test set accuracy was $R = 0.99328$.

From the prediction results obtained using the test set, as shown in Figs. 3(a)–3(c), the RBF algorithm's prediction curve exhibited significant oscillations, while the SVR algorithm's prediction points showed systematic deviations from the true values. In contrast, only the BPNN algorithm's prediction curve closely matched the true values. The performance on the test set was generally consistent across these observations: the RBF algorithm demonstrated severe underfitting, indicating poor generalization ability; the SVR algorithm showed a risk of overfitting; and only the BPNN algorithm exhibited optimal generalization, as depicted in Figs. 3(d)–3(f). The *R*-value scatter plots presented in Figs. 3(g)–3(i) display similar phenomena. For the RBF algorithm, the scatter points form a horizontal band, with predicted values concentrated within a narrow interval. The SVR algorithm's *R*-value scatter points are distributed along the diagonal but exhibit vertical stratification. Conversely, the BPNN algorithm's *R*-value scatter points are tightly clustered around the diagonal, and its high-density region aligns well with the true value distribution. Both the RBF and SVR algorithms exhibited issues, including insufficient feature discrimination and prediction failures within specific intervals. Only the BPNN algorithm, achieving a correlation coefficient of 0.98, produced predictions that closely surrounded the reference line. Furthermore, its high-density region perfectly overlapped with the true value distribution, demonstrating its capability for both accurate prediction and effective reproduction of the underlying data distribution. Compared to the other two algorithms, we conclude that the BPNN data regression algorithm exhibited superior prediction performance.

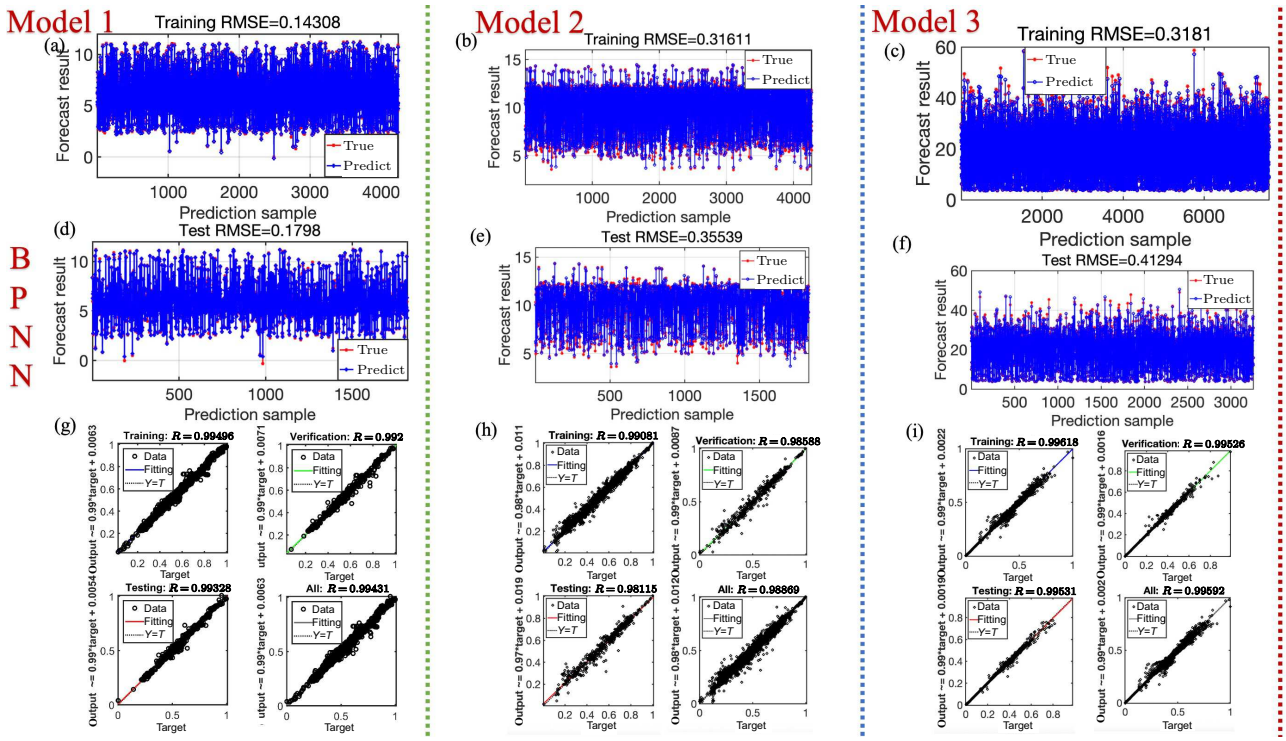


Fig. 4. RMSE and *R* values for the predictions of the BPNN algorithm based on the far-field radiation data sets of model 1, model 2, and model 3, respectively. (a)–(c) RMSE values for the model 1, model 2, and model 3 training sets; (d)–(f) RMSE values for the model 1, model 2, and model 3 test sets; (g)–(i) *R* values for the BPNN predictions for the model 1, model 2, and model 3 data sets.

We further investigated the far-field radiation prediction performance of the BPNN algorithm for the other two core–shell nanosphere-based nanoantennas. Specific results are presented in Fig. 4, which displays the RMSE and *R*-values of the BPNN algorithm when trained on the far-field radiation datasets of model 1, model 2, and model 3, respectively. The BPNN algorithm demonstrated effective generalization across all three model datasets. Consistently low RMSE values and *R*-value scatter plots tightly clustered around the diagonal (as shown in Fig. 4) confirm the algorithm's capability for accurate prediction and effective distribution reproduction across all models. We also analyzed the training iteration process. The BPNN algorithm underwent 519, 353, and 261 iterations for the model 1, model 2, and model 3 datasets, respectively. Figure 5 illustrates the iteration process and convergence for each model. During this process, we observed that the error curves for the BPNN algorithm exhibited a trend of gradual convergence across all three datasets. Importantly, no gradient explosion or vanishing phenomena were observed in any dataset, indicating that the learning rate settings for the BPNN algorithm were appropriate and that the update process was stable across all three datasets. Notably, the BPNN algorithm demonstrated optimal iterative characteristics with the model 3 dataset. Its rapid convergence, low validation errors, and sta-

ble gradient variations suggest that this model possesses significant advantages in terms of architecture design and hyperparameter selection. Therefore, it can serve as a benchmark model for subsequent far-field directionality optimization of core–shell nanosphere dimer nanoantennas. Furthermore, the aforementioned iterative validation process demonstrates that the BPNN algorithm can efficiently and accurately predict the far-field radiation characteristics of the three core–shell nanosphere and derived nanoantenna structures.

For comparison, we also trained the model 1, model 2, and model 3 datasets using the RBF and SVR algorithms. The resulting errors, accuracies, and training times are recorded in Table 2. All three algorithms performed best on the model 1 dataset, exhibiting relatively low errors and short training times. However, their performance deteriorated significantly on model 3, showing marked increases in both errors and training duration. This performance difference likely relates to the increasing complexity and differing data types across the models: model 1 contains far-field directivity data for the core–shell nanosphere; model 2 uses similar data for the notched core–shell nanosphere, while model 3 comprises far-field front-to-back ratio data for core–shell dimers. Predicting the front-to-back ratio for the more complex dimer structure (model 3) is inherently more challenging. Table 2 clearly demonstrates that the BPNN algorithm outperforms both the RBF and SVR algorithms. The BPNN algorithm achieves the lowest error, shortest training time, and highest accuracy (exceeding 99%) across all tested models.

During the BPNN algorithm training, we also observed that the prediction error depends on the number of hidden layers employed. Figure 6 illustrates this relationship by plotting the error trend versus the hidden layer count for the BPNN algorithm trained on the model 1, model 2, and model 3 datasets. The fundamental principle of the BPNN algorithm involves a learning process divided into two phases: forward propagation and backward propagation. In the forward pass, input data (e.g., the geometric parameters of the nanoantenna) propagate sequentially through the network layers. Computations

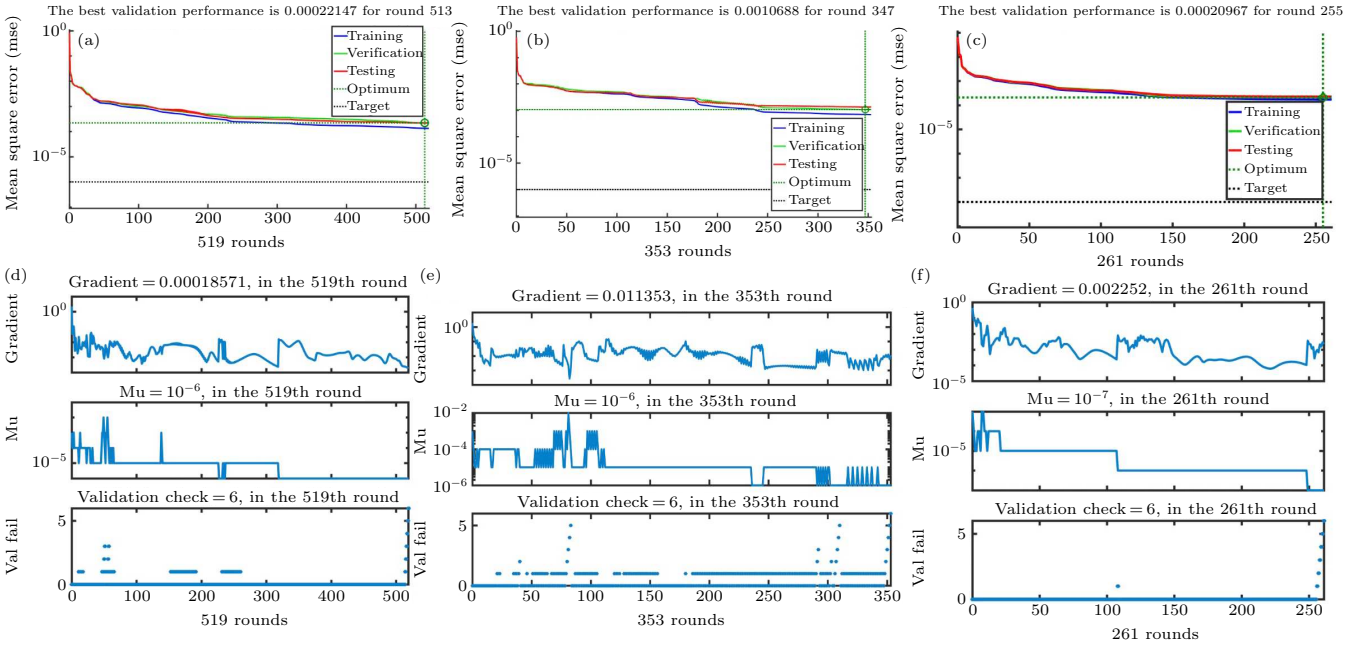


Fig. 5. Convergence and iteration when the BPNN algorithm predicts the far-field radiation data sets of model 1, model 2, and model 3, respectively. (a)–(c) Mean square errors of the model 1, model 2, and model 3 training sets; (d)–(f) iteration processes of the model 1, model 2, and model 3 test sets.

Table 2. The errors, accuracies, and training time of the RBF, SVR and BPNN algorithms for model 1, model 2, and model 3, respectively.

Model	Algorithm	Training set error (MAE)	Training set error (MBE)	Training set error (RMSE)	Test set error (MAE)	Test set error (MBE)	Test set error (RMSE)	Accuracy of training set	Accuracy of test set	Time (s)
Model 1	RBF	0.21283	0.029624	0.45393	0.25864	0.016282	0.46807	0.94216	0.93518	28.574
	SVR	0.27736	0.0011415	0.38665	0.29853	0.0031622	0.37977	0.95707	0.95044	38.72
	BPNN	0.10038	0.00096157	0.14308	0.11597	0.0065716	0.1798	0.99496	0.99328	45.112
Model 2	RBF	0.37578	0.049799	0.59901	0.44992	0.014143	0.69163	0.91967	0.89142	29.148
	SVR	0.31025	0.01669	0.59509	0.35813	0.003597	0.68495	0.92003	0.91405	36.384
	BPNN	0.21945	0.0014521	0.31611	0.23906	0.009817	0.35539	0.99081	0.98115	28.618
Model 3	RBF	0.3845	0.015728	0.82366	0.39987	0.0063474	0.87652	0.89621	0.87405	52.8
	SVR	0.35084	0.059712	0.77562	0.39331	0.060331	0.82043	0.91307	0.89619	284.764
	BPNN	0.23814	0.0039628	0.3181	0.33548	0.0029153	0.41294	0.99618	0.99531	57.256

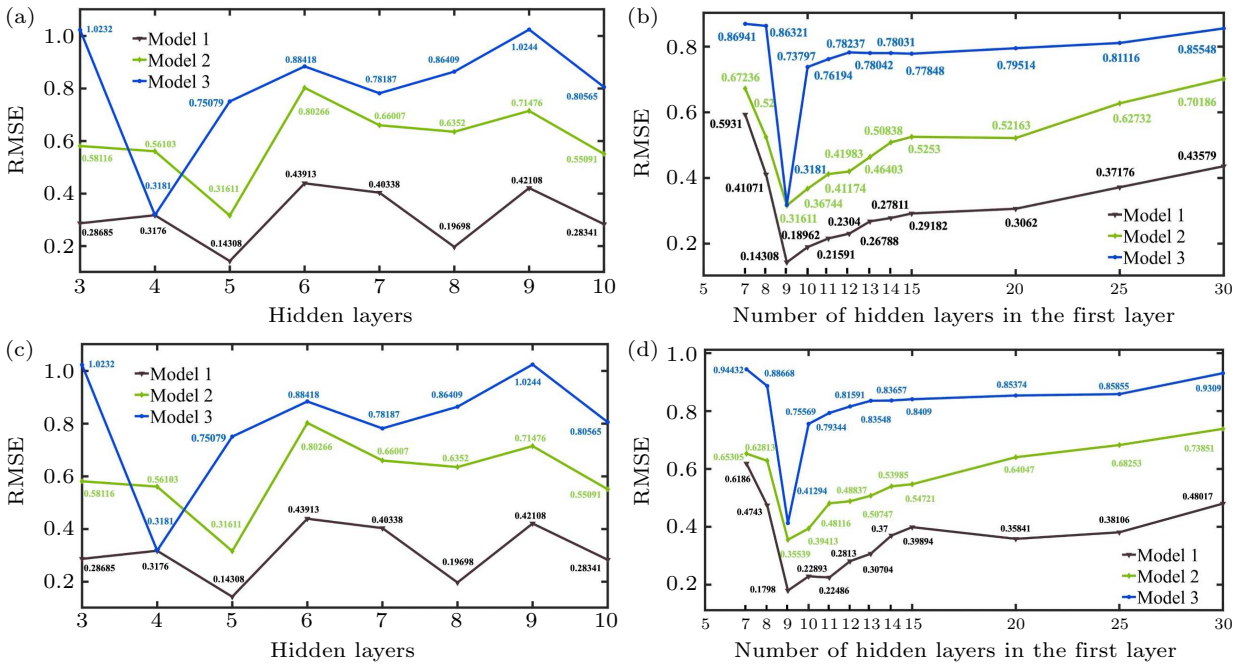


Fig. 6. Predictions of the BPNN algorithm for the errors in the number of hidden layers (a), (c) and the numbers of layers in the first hidden layer (b), (d) in the far-field radiation data sets of model 1, model 2, and model 3, respectively.

within each layer transform the data, ultimately yielding a predicted output (e.g., far-field directivity or front-to-back ratio). In the subsequent backward propagation phase, this predicted value is compared against the actual (true) value to calculate an error signal. This error signal is then propagated backward through the network, layer by layer. Based on this error, an optimization algorithm (such as gradient descent) adjusts the connection weights between neurons to minimize the error in future predictions.

Compared to the RBF and SVR algorithms, the BPNN algorithm offers greater flexibility for parameter optimization by allowing adjustment of both the number of hidden layers and the number of neurons per layer. This enables fine-tuning of the network complexity to accurately model the input–output relationship and improve prediction accuracy. To tune the network architecture, we first employed an incremental approach for determining the number of hidden layers. We observed RMSE changes as the layer count increased from three to ten for each dataset (model 1, model 2, and model 3), with the results shown in Figs. 6(a) and 6(b). Subsequently, we used a decremental method to determine the optimal neuron count for the first hidden layer, monitoring RMSE trends as this count was reduced from 30 down to seven (Figs. 6(c) and 6(d)). Based on minimizing the RMSE on both the training and test sets (Figs. 6(a) and 6(b)), the optimal numbers of hidden layers were determined to be five for model 1 and model 2 and four for model 3. Analysis of the first hidden layer's neuron count (Figs. 6(c) and 6(d)) indicated that the lowest training and test RMSE values occurred with nine neurons across all datasets. Employing a strategy of progressively decreasing neuron counts in subsequent hidden layers, the final optimal architectures were identified as follows: [9, 8, 7, 6, 4] neurons distributed across five layers for model 1 and model 2, and [9, 8, 7, 5] neurons distributed across four layers for model 3.

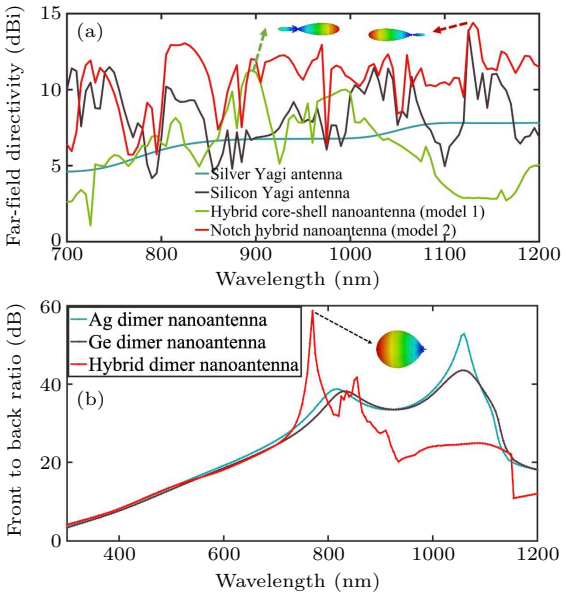


Fig. 7. Far-field radiation characteristic curves for model 1, model 2, and model 3. (a) Far-field directivity of model 1, model 2, and silver and silicon Yagi array nanoantennas under quantum source excitation. (b) Radiation before and after excitation of model 3 and silver and germanium dimers under quantum source excitation.

Using these optimized BPNN architectures, we determined the optimal geometric parameters for each nanoantenna type (model 1, model 2, and model 3) and the ideal placement distance for the quantum emitter relative to the antenna. The resulting far-field radiation patterns for the three optimized nanoantenna systems are shown in Fig. 7. This figure also compares these patterns to those of equivalent single-

material nanoantennas, clearly demonstrating that the core–shell structures exhibit superior directivity. Notably, the optimized notched core–shell antenna (model 2) demonstrates good directivity when compared to benchmark silver and silicon Yagi–Uda arrays (Fig. 7(a)). Similarly, the optimized core–shell dimer antenna (model 3) exhibits strong directivity compared to single-material dimers, achieving a front-to-back ratio exceeding 60 at a wavelength of 750 nm (Fig. 7(b)). These results demonstrate that modifying a single multilayer core–shell nanosphere (by notching or dimerization) can effectively control quantum emitter radiation directionality. This control arises from the excitation of higher-order electric and magnetic multipoles with opposite phases.

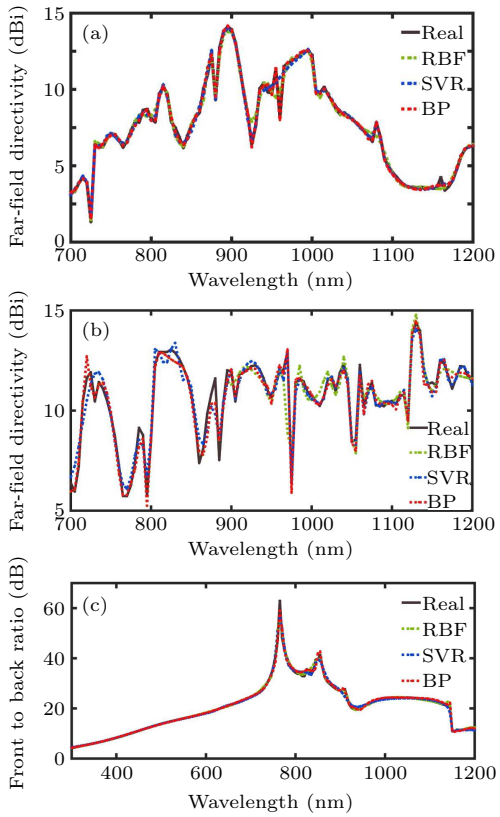


Fig. 8. Comparison of far-field radiation characteristics predicted by three regression algorithms for three radiation systems composed of a quantum source and core–shell nanospheres (model 1, model 2, and model 3) and their derived nanoantennas. (a) Comparison of the predicted radiation directionality of model 1 with actual values for three regression algorithms. (b) Comparison of the predicted radiation directionality of model 2 with actual values for three regression algorithms. (c) Comparison of the predicted front-to-back ratio of model 3 with actual values for three regression algorithms.

Finally, we compared the far-field predictions from the three regression algorithms (RBF, SVR, and BPNN) against the actual simulation results for the model 1, model 2, and model 3 antenna systems. Figure 8 presents scatter plots of these predicted versus actual values for each algorithm. These plots visually confirm that the BPNN significantly outperforms both the RBF and SVR algorithms. The BPNN demonstrates superior accuracy, as evidenced by the fact that its data points cluster tightly around the ideal prediction line ($y = x$), indicating effectively minimized prediction errors.

In essence, the BPNN algorithm is more suitable for this nanoantenna task primarily because it excels at modeling the complex, high-dimensional, nonlinear relationships inherent in nanoantenna physics. This enables it to efficiently handle large datasets and serve as a rapid, accurate surrogate model, which is crucial for optimization. Consequently, BPNN offers a superior overall balance of adaptive feature learning, predictive accuracy, generalization, and manageable computational cost for this specific application compared to alternatives like RBF or SVR.

3. Conclusion

Traditional nanoantenna design faces challenges, including high computational costs and optimization difficulties for complex targets. Addressing these issues, our paper introduced a novel method employing neural networks — specifically RBF, SVR, and BPNN — to efficiently optimize single core–shell nanosphere antennas and their derivatives (notched and dimer structures). We investigated the relationship between antenna geometry, quantum emitter position, and far-field response. A performance comparison showed that the BPNN offered superior error control and shorter training times. Using the optimized BPNN, we determined ideal geometric parameters and emitter positions for the nanoantennas. Under these optimized conditions, all three structures effectively controlled quantum emitter radiation directionality. Notably, the optimized notched core–shell antenna achieved a directivity of 14, surpassing typical Yagi–Uda arrays, while the core–shell dimer exhibited a front-to-back ratio exceeding 60 at 750 nm, outperforming single-material dimers. These results validate that structural modifications (notching, dimerization) combined with BPNN optimization enable the excitation of higher-order multipoles with opposite phases, leading to strong directional control. This methodology offers a promising direction for the design of complex, high-performance nanophotonic devices.

Acknowledgments

Project supported by the Key Research Projects of Colleges and Universities in Anhui Province (Grant No. KJ2021A0492), the Pre-research Project of the National Natural Science Foundation, AnHui Polytechnic University (Grant Nos. Xjky2022042 and Xjky2022048), the Testing Technology and Energy Saving Device Anhui Provincial Laboratory Open Fund (Grant No. JCKJ2022A09), the Joint Opening Project of Anhui Engineering Research Center of Vehicle Display Integrated Systems and Joint Discipline Key Laboratory of Touch Display Materials and Devices in An-

hui Province (Grant No. VDIS2023B02), and the Science and Technology Project of Wuhu (Grant No. 2023jc05).

References

[1] Zeng W, Jin Y, Zhou R, Li Y and Chen H 2024 *Chem. Eng. J.* **482** 148994
[2] López-Fernández I, Valli D and Wang C Y 2024 *Adv. Funct. Mater.* **34** 2307896
[3] Chen Y, Wang S and Zhang F 2023 *Nat. Rev. Bioeng.* **1** 60
[4] Sun Y, Wu J and Li Y 2023 *IEEE J. Sel. Top. Quantum Electron.* **29** 1
[5] Fang S and Hu Y H 2022 *Chem. Soc. Rev.* **51** 3609
[6] Guidry M A, Lukin D M and Yang K Y 2022 *Nat. Photonics* **16** 52
[7] Savelev R S, Sergaeva O N and Baranov D G 2017 *Phys. Rev. B* **95** 235409
[8] Kar N, McCoy M and Wolfe J 2024 *Nat. Synth.* **3** 175
[9] Zhou Y, Lu Y and Liu Y 2023 *Biosens. Bioelectron.* **228** 115231
[10] Ammari H, Li B and Zou J 2023 *Trans. Am. Math. Soc.* **376** 39
[11] Krasnok A E, Simovski C R and Belov P A 2014 *Nanoscale* **6** 7354
[12] Jiang L, Fang B and Yan Z 2020 *Microw. Opt. Technol. Lett.* **62** 2405
[13] Limonov M F, Rybin M V and Poddubny A N 2017 *Nat. Photonics* **11** 543
[14] Hu D C, Wang J and Dong Q X 2023 *ACS Appl. Nano Mater.* **6** 16856
[15] Wekalao J, Elsayed H A and El-Sherbeeny A M 2025 *Plasmonics* 1
[16] Wu Q, Li X and Jiang L 2021 *Opt. Mater. Express* **11** 1907
[17] He J, He C, Zheng C and Wang Q 2019 *Nanoscale* **11** 17444
[18] Wiecha P R and Muskens O L 2019 *Nano Lett.* **20** 329
[19] Jiang Q, Zhu L, Shu C and Sekar V 2022 *Neural Comput. Appl.* 1
[20] Shi L, Zhang Q and Zhang S 2021 *IEEE J. Multiscale Multiphys. Comput. Tech.* **6** 50
[21] Wang Z, Qin J and Hu Z 2022 *Appl. Sci.* **12** 12543
[22] Yarotsky D 2017 *Neural Netw.* **94** 103
[23] Vinatoru M, Mason T J and Calinescu I 2017 *TrAC Trends Anal. Chem.* **97** 159
[24] Dubrovskii V G 2022 *Nanomaterials* **12** 253
[25] Hodson T O 2022 *Geosci. model Dev. Discuss.* 1
[26] Namasudra S, Dhamodharavadhani S and Rathipriya R 2023 *Neural Process. Lett.* 1